JACS
JOURNAL OF THE AMERICAN CHEMICAL SOCIETY

Article

pubs.acs.org/JACS

Multiwalled Carbon Nanotubes Drive the Activity of Metal@oxide Core–Shell Catalysts in Modular Nanocomposites

Matteo Cargnello,[†] Marek Grzelczak,[†] Benito Rodríguez-González,[‡] Zois Syrgiannis,[†] Kevin Bakhmutsky,[§] Valeria La Parola,[#] Luis M. Liz-Marzán,[‡] Raymond J. Gorte,[§] Maurizio Prato,*[,†] and Paolo Fornasiero*[,†]

[†]Department of Chemical and Pharmaceutical Sciences, INSTM, Center of Excellence for Nanostructured Materials (CENMAT), University of Trieste, Via L. Giorgieri 1, 34127 Trieste, Italy

[‡]Departamento de Química Física, Universidade de Vigo, 36310 Vigo, Spain

[§]Department of Chemical and Biomolecular Engineering, University of Pennsylvania, 311A Towne Building, 220 South 33rd Street, Philadelphia, Pennsylvania 19104, United States

[#]Istituto per lo Studio dei Materiali Nanostrutturati (ISMN-CNR), Via Ugo La Malfa 153, Palermo I-90146, Italy

Supporting Information

ABSTRACT: Rational nanostructure manipulation has been used to prepare nanocomposites in which multiwalled carbon nanotubes (MWCNTs) were embedded inside mesoporous layers of oxides (TiO_2, ZrO_2, or CeO_2), which in turn contained dispersed metal nanoparticles (Pd or Pt). We show that the MWCNTs induce the crystallization of the oxide layer at room temperature and that the mesoporous oxide shell allows the particles to be accessible for catalytic reactions. In contrast to samples prepared in the absence of MWCNTs, both the activity and the stability of core–shell catalysts is largely enhanced, resulting in nanocomposites with remarkable performance for the water–gas-shift reaction, photocatalytic reforming of methanol, and Suzuki coupling. The modular approach shown here demonstrates that high-performance catalytic materials can be obtained through the precise organization of nanoscale building blocks.

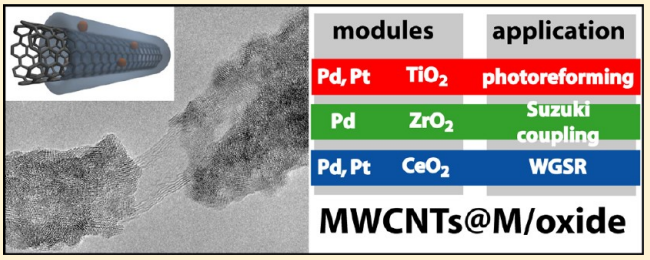

INTRODUCTION

The ability to build hierarchical structures by arranging different building blocks with nanometer-scale precision is one of the most useful aspects of nanotechnology.[1,2] This concept can produce novel materials with properties that are different from those expected from the simple sum of the individual blocks.[3] Indeed, the interactions between the constituent parts in nanometer-scale ensembles can lead to novel electronic, optical, or catalytic properties not available in the initial building blocks.[4] In the field of heterogeneous catalysis in particular, the interactions between the active phase, supports, and promoters is critical for obtaining high performance materials. These interactions can be both electronic and geometric. Furthermore, the demands in terms of geometry and binding energy of the active sites for different catalytic reactions can be very different.

In particular, carbon nanotubes (CNTs) and multiwalled carbon nanotubes (MWCNTs) have emerged as highly beneficial building blocks for the preparation of various composites. For example, hybrids of CNTs and inorganic materials have received great attention for applications in gas sensing, photovoltaics, and catalysis.[5] The main advantages of using CNTs as substrates for the formation of nanocomposites are their large surface-to-volume ratio, excellent mechanical, electrical, and optical properties, and good electrical and thermal conductivity. CNTs can also be functionalized with organic groups at different sites within their structure,[6] thereby modifying their solubility in organic solvents. Another advantage is that electronic interactions between CNTs and surrounding particles or layers can result in enhanced performance.[7,8]

Three general approaches are commonly used to prepare CNT–inorganic hybrids: (1) filling approaches, where species are placed inside the nanotube channels; (2) ex-situ methods, where preformed building blocks (e.g., metallic particles) are attached to the nanotubes via chemical bonding interactions; and (3) in situ methods, where the inorganic component is simply synthesized in the presence of the pristine or functionalized CNTs.[5] Both of the latter approaches have advantages and disadvantages. Ex-situ methods have the advantage of producing materials with tailored properties because they allow a better control on the size and the morphology of the building blocks. With in situ approaches, it is easier to manipulate the materials and the number of synthetic steps is lower.

For these reasons, composites of CNTs with catalytic metals and metal oxides have been the subject of many studies.[9−11]

Received: May 7, 2012

   dx.doi.org/10.1021/ja304398b | J. Am. Chem. Soc. XXXX, XXX, XXX−XXX

Metals supported on CNTs with CeO_2,[12−18] TiO_2,[19−22] and ZrO_2[23] have been prepared through sol−gel, hydrothermal, or electrodeposition procedures (see also ref 5 and references therein). All these methods allow the production of materials with an onion-type structure, in which the CNTs are covered by oxide layers that in turn have metal particles on the external surface. The resulting catalysts have shown promising properties in several applications.

Here, we describe the fabrication of MWCNTs covered with layers of mesoporous oxides that in turn contain embedded metal particles. As building blocks, we used oxidized MWCNTs, functionalized metallic particles, and a metal alkoxide, in a combination of ex-situ and in situ methods (Scheme 1). Specifically, the resulting hierarchical nano-

Scheme 1. Schematic Representation of the Preparation of MWCNTs@M/Oxide

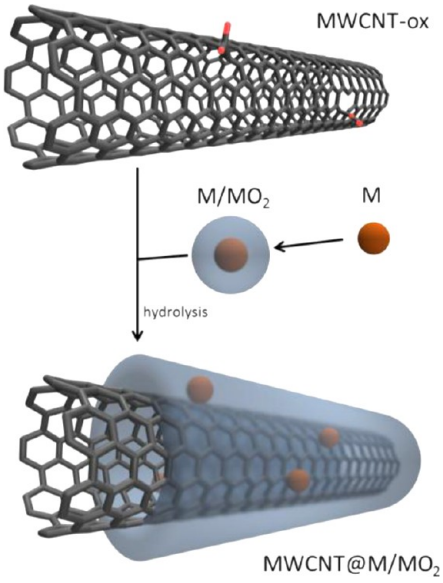

composite is formed of core−shell metal@oxide particles[24−26] supported on conducting MWCNTs.[5] The approach is highly flexible and versatile, allowing for the tuning of the composition and concentration of all the components. As a demonstration of this versatility, we prepared materials with Pd or Pt as the metallic phase, and TiO_2, ZrO_2, or CeO_2 as the metal-oxide coatings. Furthermore, we show that the thickness of the oxide layer surrounding the MWCNTs can be varied. Finally, we demonstrate that these modular composites are active and stable heterogeneous catalysts in several reactions. MWCNTs dramatically promote the activity of the materials when compared to the same metal/oxide combinations prepared in the absence of MWCNTs, for reasons that are believed to be both geometrical/morphological and electronic in nature. These materials demonstrate the utility of combining several building blocks to prepare functional nanostructures with improved performance.

EXPERIMENTAL SECTION

Materials. Titanium butoxide (97%), zirconium butoxide solution (80 wt % in 1-butanol), concentrated H_2SO_4 (95−97%), and concentrated HNO_3 (65%) were purchased from Sigma-Aldrich. MWCNTs, Nanocyl 7000, were purchased from Nanocyl s.a., Belgium.

Preparation of the Building Blocks. Pd and Pt nanoparticles protected by 11-mercaptoundecanoic acid (MUA) and cerium tetrakis(decyloxide) were prepared according to procedures described in detail elsewhere.[25,27] Oxidized MWCNTs were prepared as follows. Pristine MWCNTs (Nanocyl 7000) (150 mg) were dispersed in a concn H_2SO_4/concn HNO_3 mixture 3:1 v/v (100 mL) by sonication (6 h at 30−50 °C) and magnetic stirring (12 h at 50 °C). The suspension was washed six times by filtration; twice with water (250 mL), twice with NaOH (0.1 M, 250 mL), once with DMF (250 mL), and once with THF (250 mL). Finally, MWCNTs were redispersed in THF/DMF 5:1 v/v to a final concentration of MWCNTs of 0.5 mg mL^{-1} as carbon.

General Procedure for the Preparation of MWCNTs@M/oxide Materials. M/oxide structures were prepared by dissolving the appropriate amount of the metal alkoxide (titanium butoxide, zirconium butoxide, or cerium(IV) tetrakis(decyloxide)) in 25 mL of THF. MUA-protected Pd or Pt particles (as THF solution) were then added dropwise while stirring to avoid the precipitation of M-alkoxide networks.[25] The solution of M@oxide was then vigorously sonicated and the THF/DMF solution of oxidized MWCNTs was added simultaneously. A precipitate was formed almost immediately for all the cases, leaving a colorless supernatant, which was taken as evidence that the M@oxide structures had completely adsorbed/reacted with the MWCNTs. A mixture of H_2O (1 mL) and THF (10 mL) was added to ensure the complete hydrolysis of the alkoxide precursor, and the mixture was sonicated for an additional 15 min. The solids were then recovered by centrifugation (4500 rpm for 15 min) and washed with THF (30 mL portions) three times. The final materials were then dried at 120 °C overnight prior to being used.

Characterization Techniques. TEM measurements were performed on a TEM Philips EM208, using an acceleration voltage of 100 kV. Samples were prepared by drop casting from the dispersion onto a TEM grid (200 mesh, copper, carbon only). High resolution TEM (HRTEM) and analytical TEM studies were performed with a JEOL JEM 2010 FEG-TEM operating at an acceleration voltage of 200 kV. X-ray energy-dispersive spectra (EDS) were acquired using an Inca Energy 200 TEM system from Oxford Instruments, and electron energy loss spectroscopy (EELS) filtered TEM mappings were performed with the help of a Quantum Gatan imaging filter (GIF). Background subtraction was carried out prior to jump ratio mapping overlap. The X-ray photoelectron spectroscopy (XPS) analyses were performed with a VG Microtech ESCA 3000Multilab, equipped with a dual Mg/Al anode. The spectra were excited by the unmonochromatized, Mg Kα source (1253.6 eV) run at 14 kV and 15 mA. The analyzer was operated in the constant analyzer energy (CAE) mode. For the individual peak energy regions, a pass energy of 20 eV was set across the hemispheres. Survey spectra were measured with a 50 eV pass energy. The sample powders were analyzed as pellets, mounted on a double-sided adhesive tape. Contact of the samples with air was minimized during sample loading. The pressure in the analysis chamber was of the order of 10^{-8} Torr during data collection. The charging of the samples was removed by referencing all the energies to the C 1s set at 285.1 eV, arising from the adventitious carbon. The invariance of the peak shapes and widths at the beginning and at the end of the analyses ensured absence of differential charging. Analyses of the peaks were performed with the software provided by VG, based on nonlinear least-squares fitting program using a weighted sum of Lorentzian and Gaussian component curves after background subtraction according to Shirley and Sherwood.[28,29] Atomic concentrations were calculated from peak intensity using the sensitivity factors provided with the software. The binding energy values are quoted with a precision of ±0.15 eV and the atomic percentage with a precision of ±10%. UV−vis characterization was carried out with a Cary 5000 spectrophotometer using 10 mm path length quartz cuvettes. TGA of approximately 1 mg of each compound was recorded on a TGA Q500 (TA Instruments) under air, by equilibrating at 100 °C, and following a ramp of 10 °C min^{-1} up to 1000 °C. Raman spectra were recorded with an Invia Renishaw microspectrometer (50) equipped with He−Ne laser at 633 nm. Powders were directly placed onto a glass slide and at least 5 spectra per sample were recorded in order to check the uniformity of the materials. N_2 physisorption experiments were carried out on a Micromeritics ASAP 2020C. The

dx.doi.org/10.1021/ja304398b | J. Am. Chem. Soc. XXXX, XXX, XXX−XXX

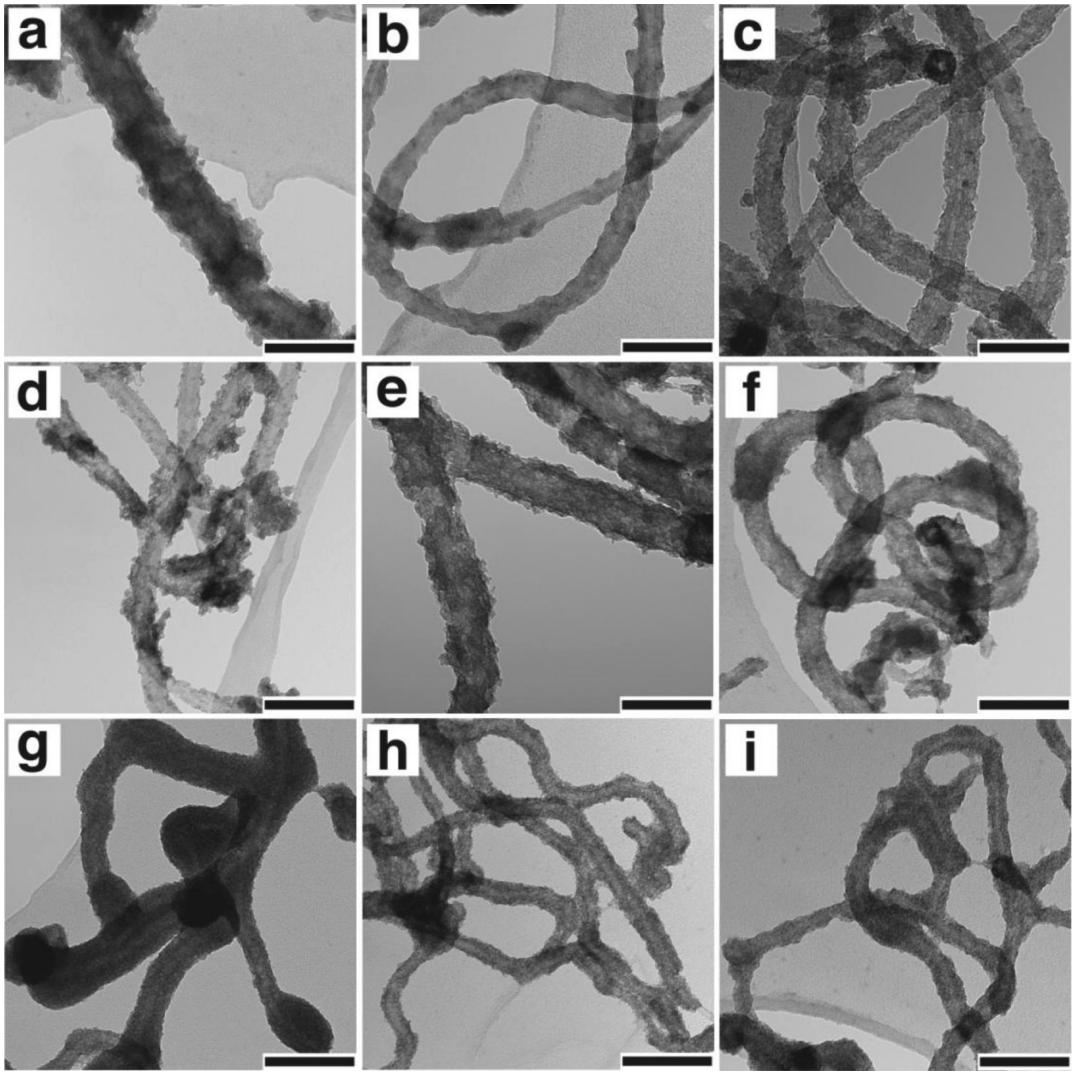

Figure 1. Representative TEM images of MWCNTs@(1 wt %)Pd−oxide nanocomposites with titania (a−c), zirconia (d−f) and ceria (g−i) shells. The weight concentration of MWCNTs is 5% (g), 10% (a, d, h), 15% (b, e, i), and 20% (c, f). All scale bars represent 100 nm.

samples were first degassed in vacuum at 120 °C overnight prior to N_2 adsorption at liquid nitrogen temperature.

Catalytic Experiments. The photocatalytic activity for H_2 production was evaluated using a 250 mL Pyrex discontinuous batch reactor with an external cooling jacket. A nominal 10 mg of catalyst was loaded in the reactor, sonicated, and dispersed under vigorous stirring into 80 mL of a water/methanol mixture (1/1 by volume). All experiments were carried out at 20 °C, and 15 mL min^{-1} of Ar were passed through the solution to transport the gaseous/volatile products to a GC for quantitative analysis. A 125 W medium pressure mercury lamp (Helios Italquartz) with Pyrex walls was used for UV−vis excitation. Gaseous products were analyzed by GC analysis using a thermal conductivity detector (TCD) and a flame ionization detector (FID) for the quantification of H_2 and CO_2.

Suzuki coupling experiments were performed as follows. Iodobenzene (1.0 mmol), phenylboronic acid (1.3 mmol), NaOH (1.5 mmol), and naphthalene (0.5 mmol as internal standard) were codissolved in 5 mL of ethanol. The mixture was stirred and heated up to 75 °C, then the catalyst (0.05 mol % as Pd with respect to iodobenzene) was added, at which point the reaction started. No biphenyl yield was obtained in the absence of the catalyst. Reagent conversions and product yields were determined by GC−MS analysis using naphthalene as internal standard. The mixtures were analyzed using an Agilent 7890 GC mounting a J&W DB-225 ms column (60 m, ID 0.25 mm, 250 μm) and coupled with an Agilent 5975 MS.

For the water−gas shift-reaction (WGSR), all catalytic tests were conducted at atmospheric pressure. The fresh catalysts were pretreated in flowing Ar at 40 mL min^{-1} for 30 min at 450 °C, after heating from room temperature at 10 °C min^{-1}. No other activation procedures (e.g., reduction) were necessary since the catalyst was reduced *in situ* under the WGS reaction conditions employed. Typically, 22 mg of fresh sample were placed in a U-shaped, quartz microreactor with internal diameter of 4 mm. The total gas flow rate under reaction conditions was 27.2 mL min^{-1} to ensure a gas hourly space velocity (GHSV) of ∼75 000 mL g^{-1} h^{-1}. The feed gas for the WGS reaction was 1.0 vol % CO and 3.0 vol % H_2O, diluted in Ar. This gaseous mixture was introduced into the reactor at 250 °C for 2 h. Aging treatments were performed by heating the sample in the WGS environment at temperatures up to 450 °C for 6 h. Subsequently, the sample was cooled down to 250 °C in the WGS environment, and the activity was measured again. All heating and cooling rates were 2 °C min^{-1}. Reactants and products were analyzed using a mass spectrometer (Hyden Analytical HPR20).

■ RESULTS AND DISCUSSION

The synthesis of the MWCNTs@M/oxide structures (M = Pd, Pt; oxide = TiO_2, ZrO_2, CeO_2) involved the use of three building blocks: oxidized MWCNTs, metal nanoparticles functionalized with 11-mercaptoundecanoic acid (MUA), and

dx.doi.org/10.1021/ja304398b | J. Am. Chem. Soc. XXXX, XXX, XXX−XXX

either Ti, Zr, or Ce alkoxide (Scheme 1). The essential idea is that the functionalized metal particles and the oxidized MWCNTs are able to bind to the metal alkoxides due to the presence of carboxyl groups that displace the weak alkoxide ligands. In the first step, the M/oxide building blocks are prepared by reacting the metal particles with the metal alkoxide. Next, the M/oxide particles are connected to the MWCNTs by reacting the MWCNTs with the alkoxide linkages that remain available on the M/oxide particles. Then this supramolecular ensemble is subjected to a controlled hydrolysis of the remaining alkoxide groups in solution to obtain uniform MWCNTs@M/oxide composites. The method is easy to implement by simply placing the three building blocks in the appropriate solvent mixtures (pure THF for combining the metal particles and the alkoxides; THF/DMF in a 5:1 ratio to react MWCNTs with M/oxide modules). DMF is necessary because of the lower solubility of MWCNTs in pure THF. To ensure proper mixing of the M/oxide particles with oxidized MWCNTs, this step was performed under sonication. Effective incorporation of all the components into the final materials was confirmed by TGA (Supporting Information, Figure S1). The characterization presented here and below is limited to Pd-based systems but similar results were obtained for the Pt-based nanocomposites.

Reference samples, in which metal particles were embedded inside oxide layers, were prepared in the manner described above but in the absence of MWCNTs. MUA−Pd or MUA−Pt nanoparticles were reacted with the alkoxides and the resulting systems hydrolyzed in THF/DMF mixtures. These materials are referred to hereafter as M@oxide. It is expected that the metal particles are located under deeper layers with respect to the MWCNTs composites, as previously observed elsewhere in materials prepared using similar procedures.[30] Physisorption of N_2 revealed that all the final materials were highly porous, with surface areas of at least ∼120 m^2 g^{-1} (Table S1, Supporting Information). BET isotherms and BJH pore size distributions (Figure S2, Supporting Information) of oxidized MWCNTs show a large N_2 uptake at pore sizes of ∼10 nm which can be attributed to the filling of the MWCNTs cavities and of the spaces in between the bundles of nanotubes.[31] After deposition of the Pd/oxide layers, this large uptake dramatically decreases, likely because the oxide layer seals the MWCNTs caps, limiting the filling by N_2, and because the nanotubes are kept much more separated. However, additional mesoporosity at small pore sizes (2−5 nm) and micropores (<2 nm) are created, which can be attributed to the presence of the oxide layer. This mesoporosity accounts for the accessibility of metal particles, as evidenced by the catalytic activity displayed by the nanocomposites (see later).

The composition in the final structure could be varied easily because the solution-phase methods used to prepare the building blocks were simple. For example, the concentration of the building blocks in the composites could be adjusted by modifying the initial ratios of the starting materials during the synthesis, for example, by changing the loading of metal nanoparticles or the MWCNTs/alkoxide ratio. The thickness of the oxide layer could also be varied, as described below.

Figure 1 shows representative transmission electron microscopy (TEM) images of composites comprising 1 wt % Pd as metal, with titania, zirconia, and ceria as the oxides. The images indicate the presence of a uniform oxide layer covering the MWCNTs. The oxide thickness depended on the material but was generally 5 to 10 nm thick (Figure S3, Supporting Information). The oxide layer was observed to be smooth in the case of titania and rougher for ceria, possibly because the ceria film is composed of larger nanocrystallites (see below). In each case, a porous architecture was formed around the MWCNTs, a morphology that is expected to be advantageous for catalytic applications. Interestingly, the TEM images of the ceria-based composites demonstrated that the thickness of the ceria layer decreased as the concentration of MWCNTs was increased from 5 wt % to 15 wt % (Figure 1g−i), in agreement with the increasing availability of surface area on the MWCNTs.

A better understanding of the composite nanostructure was obtained through HRTEM characterization of the ceria-based materials (Figure 2). The nanocrystalline nature of the ceria

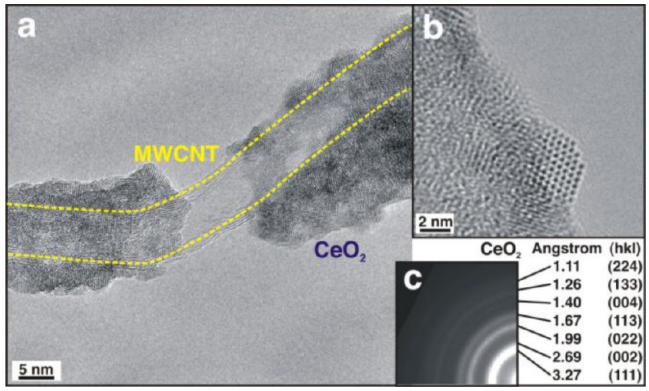

Figure 2. (a) Representative HRTEM image of MWCNTs(10 wt %)@Pd(1 wt %)/CeO_2 composites showing a partially covered MWCNT. (b) Higher magnification image showing a single CeO_2 crystallite on top of the ceria layer. (c) Electron diffraction pattern corresponding to the image in panel a, showing the reflections and the indexation on the basis of $Fm\bar{3}m$ CeO_2.

film was clearly visible, with the nanotubes being covered by small crystallites (∼4 to 5 nm, Figure 2b) of ceria, as confirmed by electron diffraction patterns (Figure 2c). Even for the thinnest ceria layer, the thickness of the oxide coating was at least 6−7 nm, on average, for the sample MWCNTs(15%)@Pd/CeO_2 (Figure S3, Supporting Information). In one instance where a partially exposed MWCNT was found (Figure 2a), the TEM images demonstrate that the rest of the MWCNT is located inside the ceria layer. The images also demonstrate that the structural characteristics of MWCNTs are maintained after the preparation of the composites, indicating that the integrity of the MWCNTs had not been altered during the formation of the composites. This fact is particularly important for retaining the electronic and mechanical properties of the MWCNTs in the final composites. A further demonstration of the core−shell nature of the MWCNTs@Pd/CeO_2 composites was provided by EELS mapping, which showed that the carbon skeleton is surrounded by a ceria layer (Figure 3).

Although the oxide layer was sometimes rough and composed of small crystallites, the layers almost always completely covered the MWCNTs. HRTEM characterization did not reveal the presence of Pd or Pt nanoparticles. This may be due to their small size (∼ 2 nm), low concentration (1 wt %), or to the fact that they were completely encapsulated by ceria, which has a rather high electron density. Indirect evidence of the complete encapsulation of all Pd in the case of unsupported Pd@ceria was obtained by EELS mapping.[25] In

dx.doi.org/10.1021/ja304398b | J. Am. Chem. Soc. XXXX, XXX, XXX−XXX

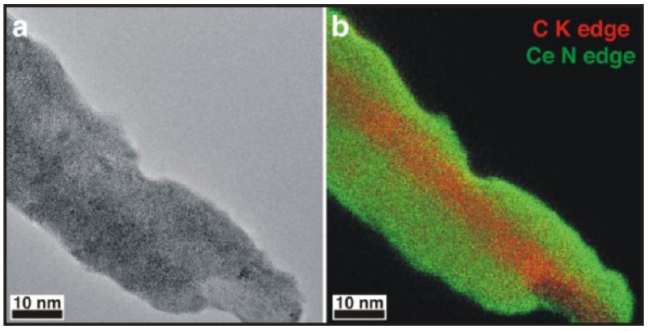

Figure 3. TEM image of a selected area of the sample (a) and corresponding EELS mapping of the C and Ce content in CNTs(10 wt %)@Pd(1 wt %)/CeO_2 composites (b) showing that the CNTs are embedded inside the ceria layer. Palladium is not visible in this image due to its very low loading.

addition, the problem of visualizing small metal particles deeply embedded within oxide layers is well-known in the case of Pt which has an even higher electron density than Pd.[24] Indeed, the presence of the metals in our samples was confirmed by EDS analysis (Figure S4, Supporting Information in the case of Pd) and XPS (see later), demonstrating that the metal−core/oxide−shell nanoparticles were effectively incorporated into the final product. In a parallel synthesis with nonfunctionalized metal particles (e.g., dodecanethiol-capped Pd or Pt particles), the metal particles were not incorporated into the nanocomposites, demonstrating that the specific interactions between the protected metal particles and the growing oxide layer were critical for incorporating the metal particles into the final composite. In the absence of these interactions, the metal nanoparticles remained in the supernatant solution after the synthesis.

Characterization by Raman spectroscopy also confirmed the contact of the oxides with the surface of MWCNTs. In the Raman spectra, the intensity ratio between the D band (indicative of disorder in the structure) and the G band (indicative of the ordered graphitic structure) is essentially unaffected by the presence of the oxide (from 1.53 to 1.55), suggesting that the incorporation of carboxyl groups on the outer graphitic shell did not seriously compromise the overall structure (Figure S5, Supporting Information). Subsequent deposition of M/oxide particles slightly decreased the D/G ratio (Figure S5, Supporting Information). Such "healing" of MWCNT by an oxide shell has been recently explained by further perturbation of outer shells with reacting oxides, leading to a decrease in the contribution of the outer graphitic shell to Raman fingerprint[32−34] Therefore, the overall Raman signal arises from the unmodified inner shell of the MWCNT, which explains the decreased D/G ratio.

In the final composites, the Raman spectra also showed peaks related to TiO_2 and CeO_2, indicating the formation of crystalline oxides, prior to any thermal treatments. In the case of ZrO_2, the absence of a Raman signal for a crystalline phase of the oxide suggests that the crystallites observed in TEM (Figure 1) might be too small and amorphous to give rise to Raman contributions. It is noteworthy that none of the M/oxide samples prepared in the absence of MWCNTs produced a

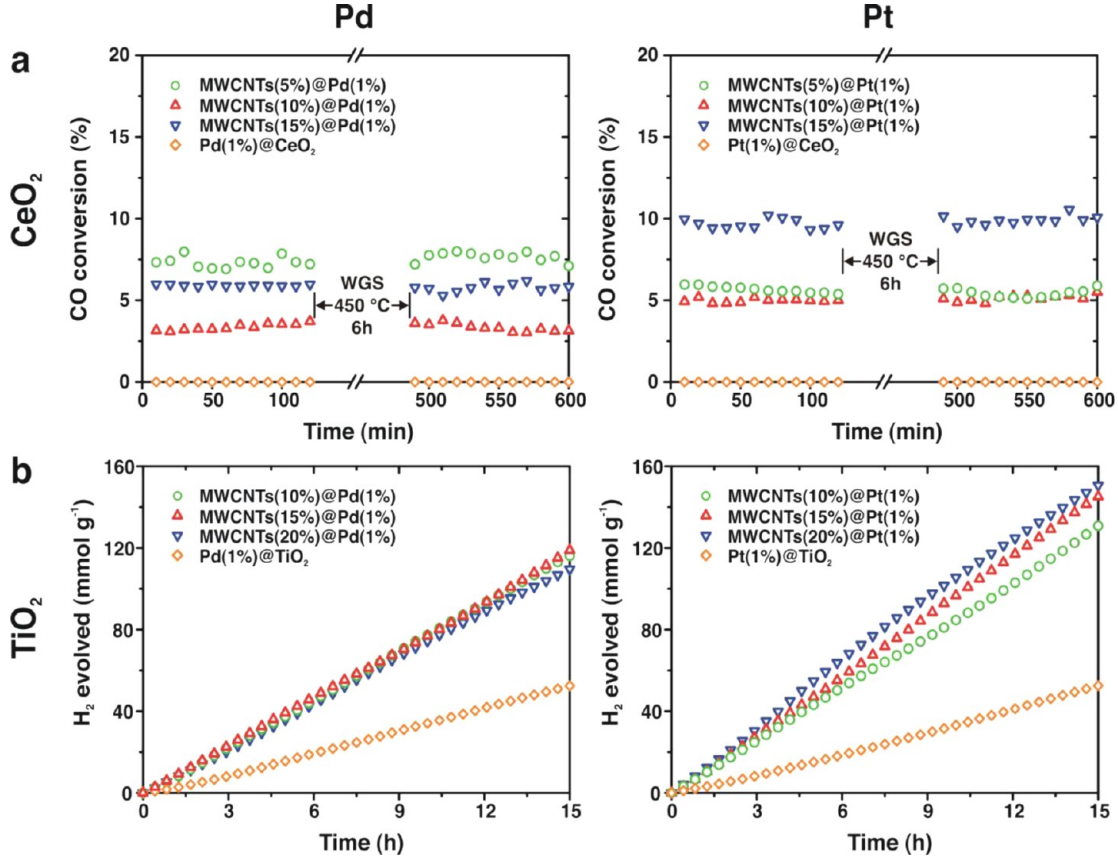

Figure 4. Catalytic activity of the different combinations of materials. (a) CO conversion during WGS reaction at 250 °C over MWCNTs@M(1%)/CeO_2. (b) photocatalytic H_2 production in the presence of methanol as sacrificial agent over MWCNTs@M(1%)/TiO_2.

dx.doi.org/10.1021/ja304398b | J. Am. Chem. Soc. XXXX, XXX, XXX−XXX

Raman signal associated with the crystalline oxides, showing that crystallization of the oxide layer was induced by the presence of oxidized MWCNTs. This suggests that the MWCNTs may exhibit a templating effect which induces the hydrolysis of the oxide precursors and confines condensation into small crystallites around the walls of the MWCNTs. The low temperature formation of metal oxides is of great advantage in catalysis since nanostructured catalysts have been shown to exhibit enhanced reaction rates.[32] The presence of nanocrystalline ceria was further demonstrated by UV−vis experiments (Figure S6, Supporting Information).

X-ray photoelectron spectroscopy (XPS) demonstrated that M/oxide and MWCNTs@M/oxide made with TiO_2 and ZrO_2 contain only Ti(IV) and Zr(IV) species (Supporting Information, Table S2 and Figures S7−S8).[35] By contrast, the XPS spectra of CeO_2-based materials revealed the coexistence of Ce(III) and Ce(IV). The content of Ce^{3+} was appreciably higher in the MWCNTs@Pd/CeO_2 nanocomposites with respect to the reference Pd@CeO_2 sample (Supporting Information, Table S2). It is known that formation of surface carbonates can lead to the presence of Ce(III). However, the higher surface area of the reference Pd@CeO_2 sample with respect to the MWCNTs@Pd/CeO_2 (Supporting Information, Table S1) suggests that the origin of the higher Ce(III) concentration might be related to a preferential formation of oxygen vacancies after embedding of the MWCNTs with ceria. This observation of interactions between the ceria and the MWCNTs agrees with previous reports of strong interactions between ceria particles deposited on graphene oxide.[36] Additionally, there was an appreciable signal for Pd in the nanocomposites containing MWCNTs, which is noteworthy because the Pd signal was absent in the Pd@CeO_2 reference material (Supporting Information, Figure S9).

We explored the catalytic behavior of the nanocomposites (MWCNTs@M/oxide) and compared their activity with reference materials (M@oxide) in selected reactions that have important implications for energy-related applications. The ceria-based structures were tested for the water−gas shift (WGS) reaction,[37] the titania-based nanocomposites were investigated for the photocatalytic production of H_2 using methanol as a sacrificial agent,[38] and the zirconia-based architectures were tested for the Suzuki coupling reaction.[39] It should be underlined that bare oxidized MWCNTs showed no activity for any of the reactions that were studied under our experimental conditions.

The WGS reaction ($CO + H_2O = CO_2 + H_2$) is important for tailoring the CO/H_2 ratio in synthesis gas, and ceria-supported group VIII metals have been shown to exhibit significantly higher rates than the same metals on inert supports such as Al_2O_3 or SiO_2.[40] The preparation of unsupported Pd@CeO_2 by a microemulsion procedure led to catalysts with poor activity, apparently due to the formation of a dense ceria barrier over the Pd that impeded the accessibility of metal particles.[30] Alumina-supported Pd@ceria particles showed good initial activity but were unstable, apparently because the ceria in the shell becomes reduced in the WGS environment, due to redox properties that are different from those of bulk ceria.[41] In agreement with these observations, Pd@CeO_2 and Pt@CeO_2 prepared in this work without the MWCNTs, as reference samples, gave no activity at 250 °C under the conditions of our present study (Figure 4, part a).

We examined the MWCNTs@ceria/Pd and MWCNTs@ceria/Pt samples for WGS showing high activity of the MWCNTs-containing samples (Figure 4, part a) and additionally, unlike the alumina-supported particles,[41] the MWCNT nanocomposites demonstrated outstanding thermal stability, even after accelerated aging under reaction conditions at 450 °C for 6 h. These results clearly indicate that the supporting skeleton (MWCNTs vs alumina) plays an important role in the stabilization of the catalytic performance.

The encapsulation of the Pd and Pt particles inside a thin and porous ceria layer has also been shown to prevent metal sintering in previous studies.[26] Considering the medium-high reaction temperature used here, the M@Ceria based systems should be equally effective in this role.[42] Therefore, the supporting MWCNTs appear to play a major role in organizing the core−shell units in a highly accessible nanoarchitecture. The fact that the Pd- and Pt-based catalysts exhibit nearly the same rates corroborates the mechanistic interpretation that the role of the metal is to activate the CO in the reaction, while ceria is responsible for water dissociation.[37]

From the photocatalytic activity standpoint, the rates for hydrogen production on MWCNTs@M/TiO_2 nanocomposites, using methanol as a sacrificial agent, were constant at 8−10 mmol h^{-1} g^{-1}, with no deactivation for up to 15 h (Figure 4, part b). MWCNTs@Pt/TiO_2 materials were slightly more active than MWCNTs@Pd/TiO_2. The high rate indirectly confirms that the titania shell must be crystalline for photoactivity, which is somewhat surprising considering that no thermal treatments have been applied to the titania shell. This also indicates that the metal particles must be accessible to protons in order to carry out the reduction to hydrogen. The activity of the Pt-based nanocomposites showed a slight dependence on the amount of MWCNTs present, whereas the Pd-based ones were not affected by this parameter. The H_2 evolution rate that we observed was higher than that found with most semiconductor photocatalysts, although the use of different conditions used for these experiments precludes a definitive comparison of activities.[43]

The most interesting aspect of these results is that the composites containing MWCNTs showed H_2 evolution rates that were 4 times higher than those of the reference Pd@TiO_2 and Pt@TiO_2 materials. Reference materials gave maximum rates for H_2 evolution of only up to 2.5 mmol h^{-1} g^{-1}. The higher activity of the MWCNT@M/TiO_2 clearly demonstrates the role of MWCNTs in enhancing the performance. This is likely due to a combination of positive effects. First, the MWCNT can delocalize the photogenerated electrons,[7,22] enhancing the lifetime of the electron hole pairs and ultimately the hydrogen evolution. Furthermore, the fact that the mechanism of enhancement does not appear to depend on the TiO_2 thickness also suggests a direct participation of the MWCNTs in light absorbance as a sensitizer.[7]

Regarding Suzuki coupling, the MWCNTs@Pd/ZrO_2 materials showed high rates for biphenyl formation (Supporting Information, Figure S10), with a quantitative yield after only a few minutes of mild heating (75 °C). The amount and thickness of the zirconia layer did not appear to affect the observed activity, further demonstrating that Pd particles alone are needed for the efficient coupling reaction. Hot filtration tests suggested that Pd leaching is not responsible for the observed activity, although it was not possible to completely rule out the role of very small amounts of leached Pd as the true active species.[44] Tests performed with the reference Pd@ZrO_2 sample showed much lower rates, indicating that the organization of the particles around the MWCNTs might be

dx.doi.org/10.1021/ja304398b | J. Am. Chem. Soc. XXXX, XXX, XXX−XXX

important for improving activity. Interestingly, the bare Pd nanoparticles show a much lower activity under similar conditions,[45] implying that a synergic enhancement of the activity is obtained through the combination of the MWCNTs and the oxide layer.

■ ASSOCIATED CONTENT

Supporting Information

TGA experiments; N_2 adsorption−desorption isotherms and corresponding BJH pore size distribution; representative HR-TEM images and associated EDS profiles; Raman, UV−vis, and XPS characterization; Suzuki cross-coupling results and additional references. This material is available free of charge via the Internet at http://pubs.acs.org.

■ AUTHOR INFORMATION

Corresponding Author

prato@units.it; pfornasiero@units.it

Notes

The authors declare no competing financial interest.

■ ACKNOWLEDGMENTS

Mr. Claudio Gamboz (University of Trieste) is acknowledged for help with TEM characterization. Dr. Valentina Gombac and Dr. Tiziano Montini (University of Trieste) are acknowledged for help with catalytic characterization. We thank the University of Trieste (FRA 2011 Project), INSTM, and MIUR (PRIN contract No. 20085M27SS and Firb RBIN04HC3S) for financial support. R.J.G. and K.B. acknowledge support from AFOSR (MURI) Grant No. FA9550-08-1-0309.

■ REFERENCES

(1) Grzelczak, M.; Vermant, J.; Furst, E. M.; Liz-Marzán, L. M. *ACS Nano* **2010**, *4*, 3591.
(2) Murray, C. B.; Norris, D. J.; Bawendi, M. G. *J. Am. Chem. Soc.* **1993**, *115*, 8706.
(3) Nie, Z.; Petukhova, A.; Kumacheva, E. *Nat. Nanotechnol.* **2010**, *5*, 15.
(4) Murray, C. B.; Kagan, C. R.; Bawendi, M. G. *Annu. Rev. Mater. Sci.* **2000**, *30*, 545.
(5) Eder, D. *Chem. Rev.* **2010**, *110*, 1348.
(6) Tasis, D.; Tagmatarchis, N.; Bianco, A.; Prato, M. *Chem. Rev.* **2006**, *106*, 1105.
(7) Woan, K.; Pyrgiotakis, G.; Sigmund, W. *Adv. Mater.* **2009**, *21*, 2233.
(8) Toma, F. M.; Sartorel, A.; Iurlo, M.; Carraro, M.; Parisse, P.; Maccato, C.; Rapino, S.; Gonzalez, B. R.; Amenitsch, H.; Da Ros, T.; Casalis, L.; Goldoni, A.; Marcaccio, M.; Scorrano, G.; Scoles, G.; Paolucci, F.; Prato, M.; Bonchio, M. *Nat. Chem.* **2010**, *2*, 826.
(9) Wildgoose, G. G.; Banks, C. E.; Compton, R. G. *Small* **2006**, *2*, 182.
(10) Pan, X.; Bao, X. *Chem. Commun.* **2008**, 6271.
(11) Banhart, F. *Nanoscale* **2009**, *1*, 201.
(12) Li, Y.; Ding, J.; Chen, J.; Xu, C.; Wei, B.; Liang, J.; Wu, D. *Mater. Res. Bull.* **2002**, *37*, 313.
(13) Bai, J.; Xu, Z.; Zheng, Y. *Chem. Lett.* **2006**, *35*, 96.
(14) Zhang, D.; Yan, T.; Shi, L.; Pan, C.; Zhang, J. *Appl. Surf. Sci.* **2009**, *255*, 5789.
(15) Zhang, D.; Pan, C.; Zhang, J.; Shi, L. *Mater. Lett.* **2008**, *62*, 3821.
(16) Zhang, D.; Shi, L.; Fu, H.; Fang, J. *Carbon* **2006**, *44*, 2853.
(17) Fiala, R.; Khalakhan, I.; Matolinova, I.; Vaclavu, M.; Vorokhta, M.; Sofer, Z.; Huber, S.; Potin, V.; Matolin, V. *J. Nanosci. Nanotechnol.* **2011**, *11*, 5062.
(18) Keyvanloo, K.; Mohamadalizadeh, A.; Towfighi, J. *Appl. Catal., A* **2012**, *417−418*, 53.
(19) Moriguchi, I.; Hidaka, R.; Yamada, H.; Kudo, T.; Murakami, H.; Nakashima, N. *Adv. Mater.* **2006**, *18*, 69.
(20) Eder, D.; Windle, A. H. *Adv. Mater.* **2008**, *20*, 1787.
(21) Liu, B.; Zeng, H. C. *Chem. Mater.* **2008**, *20*, 2711.
(22) Yu, Y.; Yu, J. C.; Yu, J. G.; Kwok, Y. C.; Che, Y. K.; Zhao, J. C.; Ding, L.; Ge, W. K.; Wong, P. K. *Appl. Catal., A* **2005**, *289*, 186.
(23) Lupo, F.; Kamalakaran, R.; Scheu, C.; Grobert, N.; Rühle, M. *Carbon* **2004**, *42*, 1995.
(24) Yeung, C. M. Y.; Yu, K. M. K.; Fu, Q. J.; Thompsett, D.; Petch, M. I.; Tsang, S. C. *J. Am. Chem. Soc.* **2005**, *127*, 18010.
(25) Cargnello, M.; Wieder, N. L.; Montini, T.; Gorte, R. J.; Fornasiero, P. *J. Am. Chem. Soc.* **2010**, *132*, 1402.
(26) De Rogatis, L.; Cargnello, M.; Gombac, V.; Lorenzut, B.; Montini, T.; Fornasiero, P. *ChemSusChem* **2010**, *3*, 24.
(27) Bakhmutsky, K.; Wieder, N. L.; Cargnello, M.; Galloway, B.; Fornasiero, P.; Gorte, R. J. *ChemSusChem* **2012**, *5*, 140.
(28) Shirley, D. A. *Phys. Rev. B* **1972**, *5*, 4709.
(29) Sherwood, P. M. A. In *Practical Surface Analysis*; Briggs, D., Seah, M. P., Eds.; Wiley: New York, 1990; p 181.
(30) Cargnello, M.; Montini, T.; Polizzi, S.; Wieder, N. L.; Gorte, R. J.; Graziani, M.; Fornasiero, P. *Dalton Trans.* **2010**, *39*, 2122.
(31) Bradley, R. H.; Cassity, K.; Andrews, R.; Meier, M.; Osbeck, S.; Andreu, A.; Johnston, C.; Crossley, A. *Appl. Surf. Sci.* **2012**, *258*, 4835.
(32) Carrettin, S.; Concepcion, P.; Corma, A.; Lopez-Nieto, J. M.; Puntes, V. F. *Angew. Chem., Int. Ed.* **2004**, *43*, 2538.
(33) Inoue, F.; Ando, R. A.; Corio, P. *J. Raman Spectrosc.* **2011**, *42*, 1379.
(34) Quintana, M.; Ke, X.; Van Tendeloo, G.; Meneghetti, M.; Bittencourt, C.; Prato, M. *ACS Nano* **2010**, *4*, 6105.
(35) Camposeco, R.; Castillo, S.; Mejia, I.; Mugica, V.; Carrera, R.; Montoya, A.; Morán-Pineda, M.; Navarrete, J.; Gómez, R. *Catal. Commun.* **2012**, *17*, 81.
(36) Joung, D.; Singh, V.; Park, S.; Schulte, A.; Seal, S.; Khondaker, S. I. *J. Phys. Chem. C* **2011**, *115*, 24494.
(37) Bunluesin, T.; Gorte, R. J.; Graham, G. W. *Appl. Catal., B* **1998**, *15*, 107.
(38) Cargnello, M.; Gasparotto, A.; Gombac, V.; Montini, T.; Barreca, D.; Fornasiero, P. *Eur. J. Inorg. Chem.* **2011**, *2011*, 4309.
(39) Miyaura, N.; Suzuki, A. *Chem. Rev.* **1995**, *95*, 2457.
(40) Hilaire, S.; Wang, X.; Luo, T.; Gorte, R. J.; Wagner, J. *Appl. Catal., A* **2001**, *215*, 271.
(41) Wieder, N. L.; Cargnello, M.; Bakhmutsky, K.; Montini, T.; Fornasiero, P.; Gorte, R. J. *J. Phys. Chem. C* **2011**, *115*, 915.
(42) Kim, J. S.; Wieder, N. L.; Abraham, A. J.; Cargnello, M.; Fornasiero, P.; Gorte, R. J.; Vohs, J. M. *J. Electrochem. Soc.* **2011**, *158*, B596−B600.
(43) Chen, X.; Shen, S.; Guo, L.; Mao, S. S. *Chem. Rev.* **2010**, *110*, 6503.
(44) Astruc, D. *Inorg. Chem.* **2007**, *46*, 1884.
(45) Cargnello, M.; Wieder, N. L.; Canton, P.; Montini, T.; Giambastiani, G.; Benedetti, A.; Gorte, R. J.; Fornasiero, P. *Chem. Mater.* **2011**, *23*, 3961.